Performance dependence of hybrid x-ray computed tomography/fluorescence molecular tomography on the optical forward problem

Damon Hyde,[1,*] Ralf Schulz,[2] Dana Brooks,[1] Eric Miller,[3] and Vasilis Ntziachristos[2]

[1]*Department of Electrical and Computer Engineering, Northeastern University, 360 Huntington Ave., Boston, Massachusetts 02115, USA*
[2]*Institute for Biological and Medical Imaging (IBMI), Technische Universität München and Helmholtz Zentrum München, Ingolstädter Landstraße 1, D-85764 Neuherberg, Germany*
[3]*Department of Electrical and Computer Engineering, Tufts University, 161 College Ave., Medford, Massachusetts 02155, USA*
*Corresponding author: dhyde@ece.neu.edu

Hybrid imaging systems combining x-ray computed tomography (CT) and fluorescence tomography can improve fluorescence imaging performance by incorporating anatomical x-ray CT information into the optical inversion problem. While the use of image priors has been investigated in the past, little is known about the optimal use of forward photon propagation models in hybrid optical systems. In this paper, we explore the impact on reconstruction accuracy of the use of propagation models of varying complexity, specifically in the context of these hybrid imaging systems where significant structural information is known *a priori*. Our results demonstrate that the use of generically known parameters provides near optimal performance, even when parameter mismatch remains. © 2009 Optical Society of America

OCIS codes: 110.0113, 110.1758.

1. INTRODUCTION

Emerging hybrid imaging systems such as x-ray computed tomography fluorescence molecular tomography (XCT-FMT) offer high resolution anatomical information in conjunction with *in vivo* quantification of cellular and subcellular tissue biomarkers [1–3]. Recent advances in data collection methodologies, modeling techniques, and image formation theory have led to small animal FMT systems that employ complete-angle 360°-projection collection geometries, use CCD camera detectors for high spatial sampling of photon fields propagating through tissue, and offer large field of view to obtain projections over large volumes.

The development of multimodal imaging methods such as XCT-FMT has been motivated largely to address fundamental limitations associated with stand-alone fluorescence systems. Specifically, the ill-posed nature of the FMT image formation problem can be significantly offset through the addition of high-resolution anatomic information from modalities such as XCT and MRI [3–7]. Such prior information can be used in both modeling and inversion, and has been shown to significantly improve image quality. Different inversion approaches have been suggested for the implementation of inverse problems with methodologies that avoid the use of hard priors offering promising characteristics in order to avoid image bias [8].

Here we investigate the forward modeling aspect of the hybrid tomographic problem. Our imaging system employs the normalized Born approximation, or Born ratio, which divides measurements at the fluorescence wave-length by corresponding measurements at the excitation wavelength [9]. This approach allows direct computation of fluorescence parameters without the intermediate determination of tissue optical properties [10]. Additionally, the Born ratio has been shown to grant a significant degree of invariance to inhomogeneities in the background optical properties of the medium. That is, the Born ratio corrects for differences between the modeled optical parameters and those present *in vivo*. Because of this correction, it is unclear whether the use of more elaborate forward models is necessary, or if forward model simplifications will be sufficient to obtain near optimal results.

Additionally, the use of prior information in the inverse problem also yields significant performance improvements in the resulting images. This raises questions regarding the interaction between structural prior knowledge in the forward and inverse problems, and to what degree inverse structural priors can compensate for simplifications of the forward model. To this end, we investigated inverse solutions both with and without structural prior for each potential forward model and examined the relative cost incurred by each subsequent model simplification.

In stand-alone FMT, where only the air–tissue surface may be known using surface extraction techniques, an internally homogeneous medium can be assumed with each optical property constant throughout the volume, and data normalization can be employed to correct for the effects of tissue optical heterogeneity [11]. For imaging of whole animals, the resulting parameter values are com-

monly set in the range of $\mu_a = 0.3$ cm^{-1} and $\mu_s' = 10$ cm^{-1} to correspond with the average values of bulk soft tissue. In contrast, the x-ray CT component of the hybrid approach provides knowledge of the internal geometry that can enable the implementation of more elaborate photon propagation models to account for the differences in absorption and scattering present within each organ or tissue. This improved modeling yields sensitivity functions that more accurately reflect the physical diffusion taking place within the animal.

However, the introduction of additional optical parameters complicates the implementation of these models. Anatomic images are frequently segmented into a number of discrete regions corresponding to individual organs or optically similar tissue types, each of which must be assigned absorption and scattering values that accurately reflect those present *in vivo*. One option for selecting these values is to explicitly calculate them through solution of the diffuse optical tomography (DOT) problem [12]. This approach is theoretically the most accurate but leads to increased complexity and additional computation requirements. Also important is that this calculation may include and therefore propagate errors to the fluorescence reconstruction problem that can bias the final fluorescence image.

An alternate approach that can be employed when constructing forward models for optical tomography is to employ average parameter values from published or measured ranges for the different tissue types segmented on the CT image. While perhaps not as accurate as explicit parameter estimation on a per animal basis, this limitation may be offset by the simplicity and lack of additional computation. What remains to be established is the trade-off in terms of reconstruction accuracy that results from having a mismatch in modeled issue optical parameters.

2. METHODS

To examine the effects of parameter selection on the resulting solutions, we assumed a three-dimensional geometry representative of the murine chest, as illustrated in Fig. 1(a). This geometry was based on an *in vivo* x-ray CT of a nude mouse segmented to differentiate heart, lung, liver, and bone from surrounding soft tissue. It is thus both physically realistic and representative of geometries for *in vivo* multimodal imaging of the chest cavity, a region that presents a difficult fluorescence tomography problem because of the high degree of optical inhomogeneity. Two hexahedral finite element method (FEM)
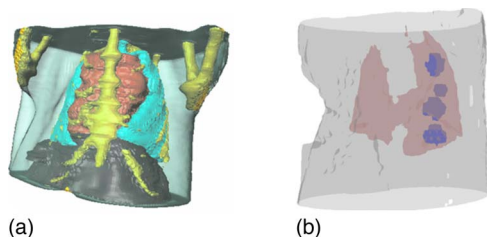

(a)   (b)

Fig. 1.   (Color online) (a) Rendering of FEM geometry. (b) Rendering showing exterior surface, lung surface, and location of all four fluorescing inclusions used in combination to generate simulated data measurements.

meshes were generated, one with approximately 64 000 nodes used for data generation and a coarser 11 000 node mesh for data inversion.

Optical parameter ranges for each tissue were obtained from existing literature (Tables 1 and 2). From these ranges, values were selected to create four models of light diffusion. We will refer to these models as the matched, mismatched, midrange, and homogeneous models. The matched model is so-called because the high-resolution model used for data generation for all cases employed the same set of tissue optical parameters. For each tissue type, the optical parameter value in the matched model was selected to be at one extreme of the associated published range. This allowed us to select optical parameters for the mismatched model at the opposite ends of each range from those selected for the matched model. Given the physically realistic ranges and the use of the matched model for data generation, this represents a worst case scenario, as the mismatch in μ_a and μ_s' was maximized with respect to values used for data generation.

The midrange model used values at the center of their corresponding ranges. Assuming that this represents the average absorption and scattering parameters for each tissue type, this choice will on average minimize the mismatch between the model and those parameters present *in vivo*. Finally, the homogeneous model assumed that the optical parameters were uniform throughout the medium, equivalent to assuming no prior knowledge about the animal's internal structure. These values are not shown in the tables, and were set to $\mu_a = 0.3$ cm^{-1} and $\mu_s' = 10$ cm^{-1} for all tissues.

Each of these four sets of model parameters was used to construct a diffusion problem on the anatomically defined FEM mesh. Using the Deal.II FEM libraries [13,14], solutions to the diffusion approximation were obtained for point sources at each of the source and detector locations. These solutions can be seen as Green's functions associ-

Table 1. Modeled and Published Values for μ_a

Value (cm^{-1})	Published Range	Model		
		Matched	Mismatched	Midrange
Tissue		0.34	0.28	0.30
Bone		0.10	0.10	0.10
Lung	0.20–0.30	0.30	0.20	0.25
Heart	0.30–0.40	0.30	0.40	0.35
Liver	0.40–0.60	0.60	0.40	0.50

Table 2. Modeled and Published Values for μ_s'

Value (cm^{-1})	Published Range	Model		
		Matched	Mismatched	Midrange
Tissue		12	10	10
Bone		20	17	20
Lung	25–35	35	25	30
Heart	20–25	20	25	23
Liver	10–15	15	10	13

ated with the diffusing system and can be used to construct the appropriate normalized Born models using the formula [9]

$$w(r_s, r_d, r) = \frac{G(r_s, r)G(r_d, r)}{G(r_s, r_d)}, \tag{1}$$

where $w(r_s, r_d, r)$ denotes the sensitivity of a measurement collected at point r_d to fluorescence at a point r given a point source of appropriate wavelength at point r_s. The function $G(r_1, r_2)$ denotes the solution to the diffusion problem at point r_2 given a point source at r_1.

Five fluorescing inclusions were constructed on this geometry differing in location and physical dimensions. In each case, the boundaries of the inclusion were defined and interior voxels given Gaussian distributed fluorescence intensities. The first simulated a situation where the fluorescent probe was spread throughout one entire lung, such as might be found when imaging lung inflammation. The remaining four targets were smaller, roughly spherical inclusions, as illustrated in Fig. 1(b). Three of these were approximately 3 mm in diameter, while the fourth had a diameter of 2 mm. Each was located at a different nonoverlapping location within the lung to cover a range of possible interference from other organs.

These inclusions were used to construct a total of 16 imaging scenarios. The first scenario consisted only of the full lung inclusion, while the remaining 15 data sets corresponded to all possible combinations of 1–4 of the smaller inclusions. For each scenario, multi-angle collection of diffuse data in a transmission geometry was assumed. At each collection angle, a 3×10 grid of source locations was defined with overall dimensions 0.8 cm $\times$ 1.8 cm. A corresponding set of detector locations was defined using a 10×10 grid of size 1.6 cm $\times$ 1.0 cm. Using 17 projections spaced evenly every 20° these values resulted in a total of 51 000 source–detector pairs. Simulated data with 10% added shot noise was generated using the fine-resolution mesh for Green's function computation and the linear model presented above.

3. RESULTS
Reconstructions for every data set–model combination were obtained by solving the Tikhonov regularized least-squares problem

$$\hat{x} = \arg\min_x \|Wx - b\|_2^2 + \lambda^2 \|x\|_2^2. \tag{2}$$

Here W is the linear system model constructed using Eq. (1) for each combination of source, detector, and voxel location. The vector x contains the fluorescence concentrations to be reconstructed, while b is the vector of collected data points. The regularization parameter λ was selected to minimize 2-norm error with the known true image.

Solution of the above minimization was implemented using 50 iterations of the LSQR algorithm [15]. Each data set was reconstructed twice: once using the full weight matrix and once using a structural prior model that constrained image values to lie solely within the lung region. The prior model was implemented by eliminating the elements of x and corresponding columns of A associated with voxels lying outside the lung region. For display purposes, the values of these voxels were then set to zero.

For each solution, 2-norm error with respect to ground truth was computed as

$$e_i = \frac{\|x_i - x_{true}\|_2^2}{\|x_{true}\|_2^2}. \tag{3}$$

These errors are plotted for the the standard and *a priori* inversion techniques in Figs. 2(a) and 2(b), respectively. In both cases, the matched model consistently provides the lowest reconstruction error with the midrange model yielding the second lowest error. For the standard reconstruction, the mismatched model also consistently outperforms the homogeneous model. When using the simple *a priori* approach, the errors obtained with each model are significantly lower than those seen with the standard solution method. However, unlike the standard approach, there are several cases—when imaging three or four of the small inclusions—where the homogeneous model yields a lower 2-norm error than the mismatched model. Additionally, the spread in errors between the different models has increased.

To give a better comparison of the relative performance gain achieved by moving to a more complex model, we also computed the error relative to the error seen with the matched forward model by
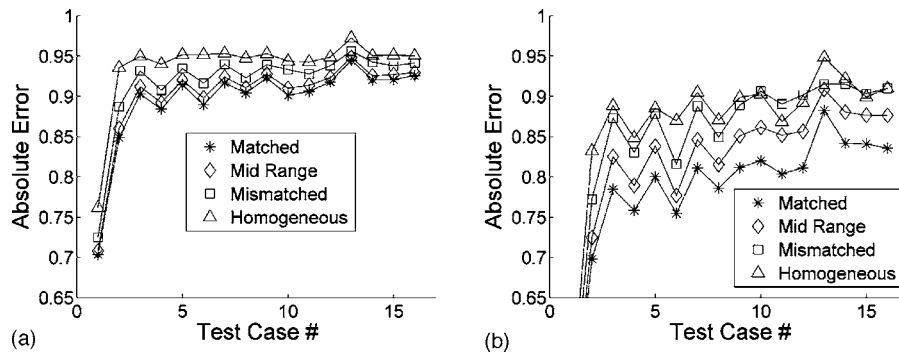

(a)

(b)

Fig. 2. Absolute 2-norm error using (a) standard and (b) *a priori* inversion. Results show consistent improvement when using midrange and matched parameter models. Error levels for the full lung inclusion incorporating *a priori* structure in the inverse problem are not shown to better display other results.
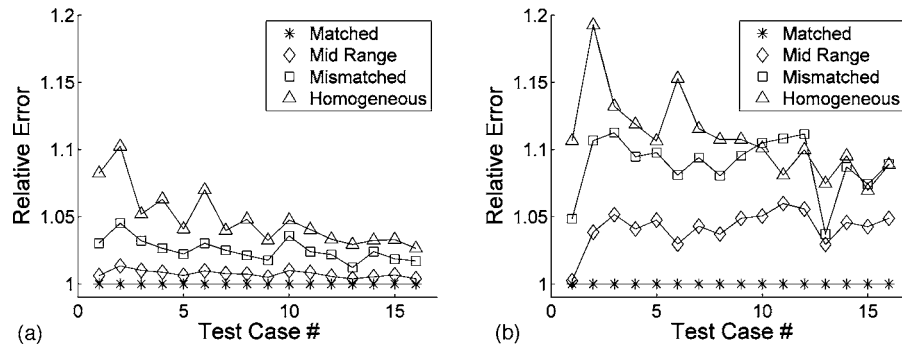
Fig. 3.   Relative 2-norm error using (a) standard and (b) *a priori* inversion. Note that relative penalty for using the incorrect model is significantly higher when using *a priori* inversion techniques.

$$e_{i,relative} = \frac{e_i}{e_{matched}}. \qquad (4)$$

These values are plotted in Figs. 3(a) and 3(b). As also seen in the absolute error plots, the homogeneous model consistently shows the largest errors when using the standard inversion approach. As more accurate model parameters are incorporated, solution error correspondingly decreases in all cases. The mismatched model offers some improvement over the homogeneous, while the midrange model consistently shows less than a 1% increase in error. Average relative error increases of 0.74%, 2.5%, and 4.8% are seen for the midrange, mismatched, and homogeneous models, respectively, as compared with the matched model.

The situation changes slightly when incorporating structural prior knowledge into the inversion process. The full fluorescing lung (Test Case #1 on the horizontal axis of Fig. 3) is reconstructed with the lowest overall error levels, as the structure of the image is provided by the prior information. When reconstructing the smaller targets, the homogeneous model yields the highest error in 12 out of 16 trials, with the mismatched model yielding the highest error for the remaining four cases. Of interest, while the use of prior information offered consistently

lower error levels, the relative penalty for using an incorrect model increased. The average relative increase in error was 4.2% for the midrange, 8.9% for the mismatched, and 10.9% for the fully homogeneous model, significantly higher than was seen without prior knowledge. These values reflect an increase in both the absolute error resulting from improper model selection and the proportion of total error. This indicates that while structural *a priori* information in the inverse problem alone can offer improved performance, the biggest gains are to be made by a combination of prior knowledge and improved diffusion modeling.

Sample reconstruction slices from the full lung target using *a priori* knowledge are shown in Fig. 4. While all models obtain the true structure of the lung, the matched and midrange models more accurately resolve the quantitative values. When reconstructing smaller inclusions, the more accurate models consistently offered improved separation of objects and lower 2-norm errors than the homogeneous and mismatched parameter models.

4. CONCLUSIONS

Our results suggest that for imaging within the murine chest, the use of established ranges for tissue optical parameters does not significantly degrade reconstruction quality even when mismatch in values remains. Furthermore, by using values from the center of the established ranges, results can be obtained that consistently offer less than a 5% increase in error as compared with using perfectly matched parameters. In contrast, the use of homogeneous models results in significantly higher error levels and reduced image fidelity. These effects are compounded when using structural information as prior knowledge in the inverse problem, which does not appear to compensate for simplified diffusion modeling. In fact, the benefits of improved diffusion modeling are greater when using inverse priors, suggesting that available structural information should always be used in the construction of the diffusion model. We conclude that the use of structural CT data in combination with published optical parameter ranges can provide improvements to diffusion modeling for fluorescence molecular tomography without the additional experimental and computational complications of explicit parameter estimation.
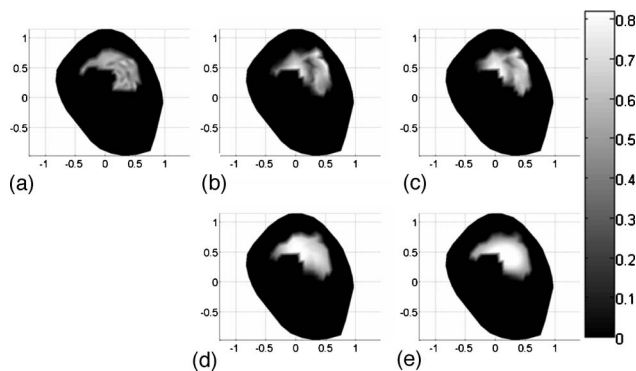

Fig. 4.   (a) True full-lung image. Reconstructions of inclusion using (b) matched model, (c) mismatched model, (d) midrange model, (e) homogeneous model.

REFERENCES

1. V. Ntziachristos, A. G. Yodh, M. Schnall, and B. Chance, "Concurrent MRI and diffuse optical tomography of breast after indocyanine green enhancement," Proc. Natl. Acad. Sci. U.S.A. **97**, 2767–2772 (2000).

2. A. Joshi, W. Bangerth, and E. M. Sevick-Muraca, "Non-contact fluorescence optical tomography with scanning patterned illumination," Opt. Express **14**, 6516–6534 (2006).

3. S. C. Davis, H. Dehghani, J. Wang, S. Jiang, B. W. Pogue, and K. D. Paulsen, "Image-guided diffuse optical fluorescence tomography implemented with Laplacian-type regularization," Opt. Express **15**, 4066–4082 (2007).

4. V. Ntziachristos, E. A. Schellenberger, J. Ripoll, D. Yessayan, E. Graves, J. Alexi Bogdanov, L. Josephson, and R. Weissleder, "Visualization of antitumor treatment by means of fluorescence molecular tomography with an annexin V-Cy5.5 conjugate," Proc. Natl. Acad. Sci. U.S.A. **101**, 12294–12299 (2004).

5. R. Barbour, S. Barbour, P. Koo, H. L. Graber, R. Aronson, and J. Chang, "MRI-guided optical tomography: Prospects and computation for a new imaging method," IEEE Comput. Sci. Eng. **2**, 63–77 (1995).

6. B. Brooksby, S. Jiang, C. Kogel, M. Doyley, H. Dehghani, J. Weaver, S. Poplack, B. Pogue, and K. Paulsen, "Magnetic resonance guided near infrared tomography of the breast," Rev. Sci. Instrum. **75**, 5262–5270 (2004).

7. P. K. Yalavarthy, B. W. Pogue, H. Dehghani, and K. D. Paulsen, "Weight-matrix structured regularization provides optimal generalized least-squares estimate in diffuse optical tomography," Med. Phys. **34**, 2085–2098 (2007).

8. M. Guven, B. Yazici, X. Intes, and B. Chance, "Diffuse optical tomography with a priori anatomical information," Phys. Med. Biol. **50**, 2837–2858 (2005).

9. V. Ntziachristos and R. Weissleder, "Experimental three-dimensional fluorescence reconstruction of diffuse media by use of the normalized Born approximation," Opt. Lett. **26**, 893–895 (2001).

10. A. Soubret, J. Ripoll, and V. Ntziachristos, "Accuracy of fluorescent tomography in the presence of heterogeneities: Study of the normalized Born ratio," IEEE Trans. Med. Imaging **24**, 1377–1386 (2005).

11. T. Lasser, A. Soubret, J. Ripoll, and V. Ntziachristos, "Surface reconstruction for free-space 360° fluorescence molecular tomography and the effects of animal motion," IEEE Trans. Med. Imaging **27**, 188–194 (2008).

12. A. B. Milstein, J. J. Stott, S. Oh, D. A. Boas, R. P. Millane, C. A. Bouman, and K. J. Webb, "Fluorescence optical diffusion tomography using multiple-frequency data," J. Opt. Soc. Am. A **21**, 1035–1049 (2004).

13. W. Bangerth, R. Hartmann, and G. Kanschat, "Deal.II—a general-purpose object-oriented finite element library," ACM Trans. Math. Softw. **33**, 24:1–24:27 (2007).

14. W. Bangerth, R. Hartmann, and G. Kanschat, Deal.II: A Finite Element Differential Equations Analysis Library, http://www.dealii.org.

15. C. Paige and M. Saunders, "LSQR: An algorithm for sparse linear equations and sparse least squares," ACM Trans. Math. Softw. **8**, 43–71 (1982).